PERGAMON

International Journal of Multiphase Flow 28 (2002) 1269–1292

International Journal of Multiphase Flow

www.elsevier.com/locate/ijmulflow

Power law correlations for sediment transport in pressure driven channel flows

N.A. Patankar [a,*], D.D. Joseph [b], J. Wang [b], R.D. Barree [c], M. Conway [d], M. Asadi [d]

[a] *Department of Mechanical Engineering, Northwestern University, 2145 Sheridan Road, Evanston, IL 60208, USA*
[b] *Department of Aerospace Engineering and Mechanics, University of Minnesota, Minneapolis, MN 55455, USA*
[c] *Barree & Associates LLC, Lakewood, CO 80235, USA*
[d] *STIM-LAB, Duncan, OK 73534, USA*

Received 7 May 2001; received in revised form 7 April 2002

Abstract

Lift forces acting on particles play a central role in many cases, such as sediment transport, proppant transport in fractured reservoirs, removal of drill cuttings in horizontal drill holes and cleaning of particles from surfaces. We study the problem of lift using 2D direct numerical simulations and experimental data. The lift-off of single particles and many particles in horizontal flows follow laws of similarity, power laws, which may be obtained by plotting simulation data on log–log plots. Data from slot experiments for fractured reservoirs is processed (for the first time) on log–log plots. Power laws with a parameter dependent power emerge as in the case of Richardson–Zaki correlations for bed expansion by drag.

1. Introduction

Transport of particles in a channel by fluids occurs in variety of settings such as sediment transport, proppant transport in oil reservoirs, removal of drill cuttings, etc. Our focus is on the problem of sand or proppant transport in hydraulic fracturing applications.

Hydraulic fracturing is a process often used to increase the productivity of a hydrocarbon well. A slurry of sand or proppants in a fluid is pumped into the well to be stimulated, at sufficient pressure to exceed the horizontal stresses in the rock at reservoir depth. This opens a vertical

* Corresponding author. Tel.: +1-847-491-3021; fax: +1-847-491-3915.
E-mail address: n-patankar@northwestern.edu (N.A. Patankar).

0301-9322/02/$ - see front matter © 2002 Published by Elsevier Science Ltd.
PII: S0301-9322(02)00030-7

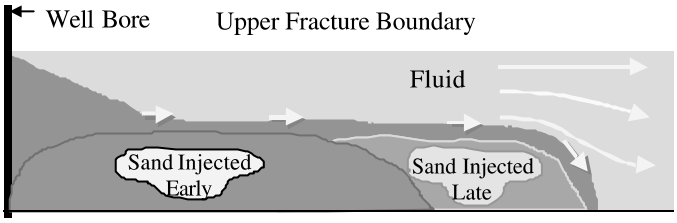

Fig. 1. Sand (proppant) transport in a fractured reservoir.

fracture penetrating from the well bore far into the pay zone. When the pumping pressure is removed, the rigid sand particles act to prop the fracture open. Productivity is enhanced because the proppant-filled fracture offers a higher-conductivity path for oil extraction.

A typical vertical fracture or crack may be 3 m high, 30 m long and 2 cm wide. The diameter of a typical sand grain is 2 mm, so that the crack width to proppant diameter ratio is about 10. The proppant density is about 2.4 g/cm^3.

Fig. 1 shows the side view of the crack. The fluid–proppant mixture is injected from the well bore. The proppants settle to the bottom as they are dragged forward. A mound of proppant develops and grows until the gap between the top of the crack and the mound reaches an equilibrium value; this value is associated with a critical condition. The velocity in the gap between the mound and the top of the slot increases as the gap size decreases. For velocities below critical the mound gets higher and spreads laterally; for larger velocities proppant is washed out until the new equilibrium height and velocity are established (Kern et al., 1959). The accumulation of proppant at the bottom causes good vertical filling to be lost. This reduces well productivity and can also interfere with the fracture growth process by blocking downward extension.

Despite many years of practice and experiments a suitable model for proppant transport or a simulation tool to predict proppant placement is yet to be fully accomplished. We have partnered with STIM-LAB (http://www.stimlab.com), a research laboratory in Duncan, OK, which is supported by a consortium of oil production and oil service companies. STIM-LAB has been collecting data on proppant transport in slots for 15 years.

The physical processes in proppant transport in fractures, described above, are settling and washout. Washout could be by sliding and slipping called the bed-load transport; however, a more efficient transport mechanism is by advection after suspension or fluidization by lift called the suspended-load transport. Lift force plays a central role in the suspension of particles in channel flows. Joseph (2002) proposed that ideas analogous to the Richardson and Zaki (1954) correlation must come into play in problems of slurries, where the particles are fluidized by lift rather than by drag. The problems of fluidization by lift can be decomposed into two separate types of study: (1) single particle studies in which the factors that govern lifting of a heavier-than-liquid particle off a wall by a shear flow are identified and (2) many particle studies in which cooperative effects on lift-off are investigated.

Direct numerical simulation (DNS) can be used to extract information implicit in the equations of fluid–particle motion. We have investigated the lift-off of a single particle and many particles in pressure driven flows by 2D DNS (Patankar et al., 2001a,b; Ko et al., in preparation; Joseph et al., 2002; Choi and Joseph, 2001). We show that the lift-off of single particles and many particles in

horizontal flows follow laws of similarity, power laws, which may be obtained by plotting simulation data on log–log plots. Power laws emerge as in the case of Richardson–Zaki (RZ) correlations for fluidization by drag. Powers laws are expected from the experimental data based on our predictions from 2D numerical simulations. The primary objective of this paper is to process the data from STIM-LAB's experiments in the same way we process data from numerical simulations. The engineering correlations for lift-off can be used to predict proppant placement in the crack.

The fracturing industry makes extensive use of numerical simulation schemes based on models and programmed to run on PC's to guide field operations. These simulations are used to predict how the fracture crack opens and closes and how proppant is transported in the crack. Commercial packages dealing with these problems and propriety packages developed by oil service companies are used extensively. These numerical schemes solve the average equations for the fluid and the proppant phases. The solid and the fluid are considered as inter-penetrating mixtures, which are governed by conservation laws. Interaction between the inter-penetrating phases is modeled. Models for drag and lift forces on the particles must be used for fluid–proppant interaction. Models for the drag force on particles in solid–liquid mixtures is a complicated issue and usually rely on the well-known Richardson and Zaki (1954) correlation. Models for lift forces in mixtures are much less well developed than models for drag. Therefore, none of the packages model the all important levitation of proppants by hydrodynamic lift. The power law models we are developing from DNS and experiments may be incorporated in the model-based simulation techniques similar to the model for drag.

The experiments of Segré and Silberberg (1962) have had a big influence on studies of the fluid mechanics of migration and lift. Eichhorn and Small (1964) performed experiments to study the lift and drag forces on spheres suspended in a Poiseuille flow. Bagnold (1974) experimentally studied the fluid forces on a body in shear flow. Ye and Roco (1992) experimentally measured the angular velocity of neutrally buoyant particles in a planar Couette flow.

Different analytical expressions for the lift force on a single particle can be found in literature. They are based on perturbing Stokes flow with inertia (e.g. Rubinow and Keller, 1961; Saffman, 1965; Bretherton, 1962; Asmolov, 1990; McLaughlin, 1991; Krishnan and Leighton, 1995 and reference therein) or on perturbing potential flow (e.g. Auton, 1987; Drew and Passman, 1999) with a little vorticity. In particular Schonberg and Hinch (1989); Hogg (1994) and Asmolov (1999) analytically studied the inertial migration of spherical particles in Poiseuille flows. The effect of curvature of the unperturbed velocity profile was found to be important. The domain of parameters for which these analytic expressions are applicable is rather severely restricted. The perturbation analyses are of considerable value because they are analytic and explicit but they are not directly applicable to engineering problems like proppant transport, removal of drill cuttings, sediment transport or even lift-off of heavy single particles.

Dandy and Dwyer (1990) and Cherukat et al. (1999) reported computational studies of the inertial lift on a sphere in linear shear flows. Mei (1992) obtained an expression for the lift force by fitting an equation to Dandy and Dwyer's (1990) data for high Reynolds numbers and Saffman's expression for low Reynolds numbers. The numerical results of Dandy and Dwyer (1990) are said to be valid for non-rotating spheres. Hence they cannot be applied, strictly speaking, to the case of freely rotating spheres in shear flows. Kurose and Komori (1999) performed numerical simulations to determine the drag and lift forces on rotating spheres in an unbounded linear shear flow.

Morris and Brady (1998) studied the migration of non-neutrally buoyant spheres in pressure driven flows of Newtonian fluids. They performed Stokesian dynamic simulations of a monolayer of spheres. These studies are valid in the creeping flow limit. In applications such as the transport of slurries or proppants, the effect of Reynolds number on the lift force is important.

A detailed investigation of the lift-off of single and many particles in channel flows at finite Reynolds numbers is necessary. In Section 3 we will review and discuss these results obtained from our 2D DNSs. New discussion on the implication of these results as compared to the RZ correlation for drag will be presented.

Shields (1936) reported one of the earliest works on modeling sediment transport. Vanoni (1975) reviews the problem of sedimentation engineering. Shields (1936) is used to predict the initial motion of sediment particles. For higher fluid flow rates the particles in the moving bed are suspended leading to transport by advection. The problem of determining the flow condition at which the suspension of the sediment begins has been addressed by Bagnold (1966); van Rijn (1984a,b); Sumer (1986) and Celik and Rodi (1991), among others. There are reasons to investigate the problem further since these studies often provide inconsistent results in determining the condition of the initiation of suspension.

In Section 2 we will discuss fluidization by drag and lift. In Section 3 we will discuss the results from DNS. The experimental setup will be described in Section 4. The correlations based on experimental data will be presented in Section 5. Conclusions will be presented in Section 6.

2. Analogy between fluidization by drag and lift

Fluidization by drag and shear is depicted in the cartoons in Fig. 2. In Fig. 2a the fluid enters at the bottom of a vertical column at a uniform fluidization velocity. At equilibrium, the drag exerted by the fluid balances the net buoyant weight of the particles. The particle bed acquires a height corresponding to the average particle fraction ϕ. When the fluidizing velocity is increased the particle bed expands. Richardson and Zaki (1954) did experiments with different fluids, particles and fluidization velocities. They plotted their data in log–log plots; miraculously this data fell on straight lines whose slope and intercept could be determined. This showed that the variables follow power laws; a theoretical explanation for this outstanding result has not been proposed. After processing the data Richardson and Zaki found that

$$V_\phi = V_0[1-\phi]^{n(R_0)}, \tag{1}$$

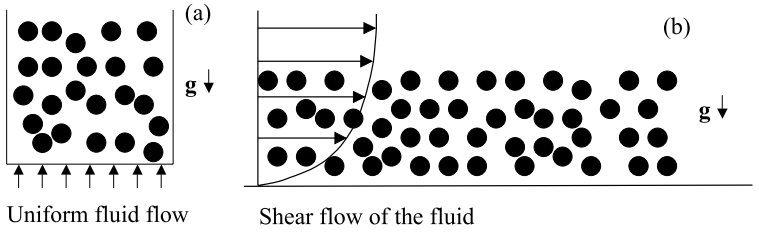

Fig. 2. (a) Heavy particles fluidized by uniform fluid flow from the bottom of a vertical column. (b) Heavy particles fluidized by lift due to shear flow of the fluid in a horizontal channel. Gravity acts vertically downwards.

where V_ϕ is the fluidization velocity at the column entrance or the composite velocity. V_0 is the "blow out" velocity, when $\phi = 0$; when $V_\phi > V_0$ all the particles are blown out of the bed. Clearly $V_\phi < V_0$ for a fluidized bed. For fluidization columns with large cross-section in comparison to the particle size, the RZ exponent $n(R_0)$ depends on the Reynolds number $R_0 = V_0 d/\nu$ only, where d denotes the particle size, e.g. diameter of a spherical particle and ν is the kinematic viscosity of the fluid. The power law in the RZ case is an example of what Barenblatt (1996) calls "incomplete self-similarity" because the power itself depends on the Reynolds number, a third parameter. Pan et al. (in press) carried out 3D DNS of the fluidization of 1204 spheres and obtained a correlation in agreement with Eq. (1). The RZ correlation gives different expressions for n for different values of R_0. In Appendix A R.D. Barree presents a way of representing the various expressions for n by a single continuous function.

Eq. (1) describes the complicated dynamics of fluidization by drag. The single particle fluidization velocity plays a key role in obtaining the fluidization velocity of concentrated suspensions. An expression for the drag force $F_\mathrm{d}(1)$ on a single isolated particle in an infinite ambient of the fluid is given by a drag law, e.g.

$$F_\mathrm{d}(1) = \begin{cases} 3\pi\eta d V_0, & \text{laminar,} \\ 0.055\pi\rho_\mathrm{f} d^2 V_0^2, & \text{turbulent,} \end{cases} \tag{2}$$

where η is the fluid dynamic viscosity, ρ_f is the fluid density and spherical particles are considered. In a fluidized bed the total force F acting on a particle is (Foscolo and Gibilaro, 1984; Joseph, 1990)

$$F(\varepsilon, R_0) = F_\mathrm{d}(\varepsilon) - F_\mathrm{B}(\varepsilon), \tag{3}$$

where ε is the fluid fraction, $F_\mathrm{d}(\varepsilon)$ is the drag on a single particle in the fluid–particle mixture and $F_\mathrm{B}(\varepsilon)$ is the effective buoyant weight of a particle in the suspension. We have, $F_\mathrm{B}(\varepsilon) = V_\mathrm{p}(\rho_\mathrm{p} - \rho_\mathrm{c})g = \varepsilon V_\mathrm{p}(\rho_\mathrm{p} - \rho_\mathrm{f})g = \varepsilon F_\mathrm{B}(1)$, where ρ_p is the particle density, V_p is the volume of the particle, g is the gravitational acceleration, $F_\mathrm{B}(1)$ is the buoyant weight of an isolated particle and $\rho_\mathrm{c} = \varepsilon\rho_\mathrm{f} + \phi\rho_\mathrm{p}$ is the effective or composite density of the fluid–particle mixture. At steady conditions

$$\begin{aligned} &F(\varepsilon, R_0) = 0, \\ &\text{i.e. } F_\mathrm{d}(\varepsilon) = F_\mathrm{B}(\varepsilon) = \varepsilon F_\mathrm{B}(1), \\ &\text{i.e. } F_\mathrm{d}(\varepsilon) = \varepsilon F_\mathrm{d}(1). \end{aligned} \tag{4}$$

For spherical particles, Eqs. (1), (2) and (4) give

$$\begin{aligned} &\left[\tfrac{\pi d^3}{6}\right]\left[\rho_\mathrm{p} - \rho_\mathrm{f}\right]g = \begin{cases} 3\pi\eta d V_\phi \varepsilon^{-n(R_0)}, & \text{laminar,} \\ 0.055\pi\rho_\mathrm{f} d^2 V_\phi^2 \varepsilon^{-2n(R_0)}, & \text{turbulent,} \end{cases} \quad \text{or} \\ &R_\mathrm{G} = \begin{cases} 18\varepsilon^{-n(R_0)} R_\phi, & \text{laminar,} \\ \left[\varepsilon^{-n(R_0)} R_\phi\right]^2, & \text{turbulent,} \end{cases} \end{aligned} \tag{5}$$

where $R_\mathrm{G} = \rho_\mathrm{f}[\rho_\mathrm{p} - \rho_\mathrm{f}]g d^3/\eta^2$ represents the Reynolds number based on the sedimentation velocity scale $V_\mathrm{G} = [\rho_\mathrm{p} - \rho_\mathrm{f}]g d^2/\eta$ and $R_\phi = \rho_\mathrm{f} V_\phi d/\eta$. Eq. (5) is another form of the correlation for fluidization by drag and can be written as

$$R_G = a(R_0) R_\phi^{p(R_0)} \varepsilon^{q(R_0)}. \quad (6)$$

Fig. 2b shows the fluidization of particles by shear flow observed in experiments and numerical simulations. At equilibrium the average lift exerted by the fluid should balance the net buoyant weight of the particles. When the applied shear rate is increased the particle bed expands. This is similar to the fluidization by drag where the mechanism for bed expansion is different. Correlations analogous to Eq. (6) may be expected for fluidization by shear. In that case a Reynolds number based on the applied shear rate should be defined instead of R_ϕ. The prefactor and the exponents may be determined from experimental or numerical data.

In the following sections we will first show that our previous DNS results are in agreement with the above expectation. New discussion based on some of our previous DNS results will be presented. We will then show that the experimental data obtained from STIM-LAB also give power law correlations.

3. Direct numerical simulation of solid–liquid flows

We used a numerical method, described in detail by Hu (1996) and Hu et al. (2001), to study the lift-off of a single particle in Newtonian and viscoelastic fluids (Patankar et al., 2001a; Joseph et al., 2002; Ko et al., in preparation). It is an Arbitrary-Lagrangian–Eulerian (ALE) numerical method using body-fitted unstructured finite element grids to simulate particulate flows. A closely related numerical method for particulate flows, based on a Chorin (1968) type fractional step scheme, was introduced by Choi (2000). Choi and Joseph (2001) and Patankar et al. (2001b) use this scheme to study the fluidization by lift of 300 circular particles in a plane Poiseuille flow by DNS.

3.1. Single particle lift-off

The principal features of lift-off and levitation to equilibrium in 2D simulations are shown in Fig. 3. A heavy particle freely translating and rotating in contact with a plane wall in Poiseuille flow is lifted from the wall and suspended in the fluid if the shear Reynolds number R is greater than a critical value. Beyond the critical shear Reynolds number the particle rises from the wall to an equilibrium height at which the buoyant weight F_B just balances the hydrodynamic lift L from the fluid. In Fig. 3, $\dot{\gamma}_w$ is the shear rate at the wall in the absence of the particle, U_p and Ω_p are the translational and angular velocities of the particle, respectively, at steady state and h_e is the equilibrium height.

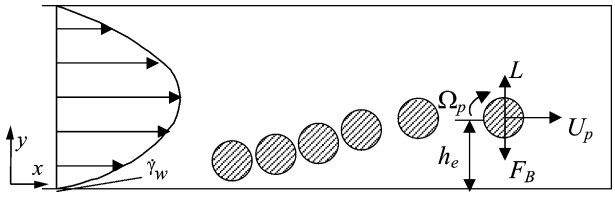

Fig. 3. Lift-off and levitation to equilibrium of a single particle.

At steady state the lift force on a freely rotating and translating circular particle in a Poiseuille flow of a Newtonian fluid depends on various parameters

$$L = f_1\left(\dot{\gamma}_w, h_e, \rho_f, \eta d, H_1\right), \tag{7}$$

where d is the particle diameter and H_1 is the channel height. At equilibrium $L = (\pi d^2/4)(\rho_p - \rho_f)g$. Using this relation and non-dimensionalizing (Buckingham's Pi theorem) we get

$$R_G = f_2\left(R, \frac{H_1}{d}, \frac{h_e}{d}\right), \tag{8}$$

where the shear Reynolds number $R = \rho_f \dot{\gamma}_w d^2/\eta$ and the gravity Reynolds number or non-dimensional lift $R_G = \rho_f(\rho_p - \rho_f)gd^3/\eta^2$. Freely moving particles in steady flow have zero acceleration. The density ratio ρ_p/ρ_f vanishes as a parameter when the particle accelerations are zero.

In practical applications the particle acquires some finite separation distance from the wall due to the presence of surface roughness. Patankar et al. (2001a) and Ko et al. (in preparation) defined the critical Reynolds number as the minimum shear Reynolds number required to lift a particle to an equilibrium height greater than $0.501d$. They reported that the effect of the channel height on the critical shear Reynolds number for $H_1/d > 12$ was not significant. At the critical condition, Eq. (8) implies that R_G should be a function of R only. The correlation that Patankar et al. (2001a) found for the lift-off of a single circular particle in a Newtonian fluid is of the form

$$R_G = aR^n, \quad a = 2.36, \ \ n = 1.39. \tag{9}$$

This is similar to the form expected from Eq. (6) and shows that self-similarity lies at the foundation of solid–liquid flows. Similar correlations were found for lift-off in Oldroyd-B fluids by Ko et al. (in preparation). There the fluid elasticity was an additional parameter. Eq. (9) was obtained for $R > 1$. In the low Reynolds number limit $n = 2$ may be expected (Leighton and Acrivos, 1985).

We found that obtaining a general expression for R_G in terms of the R, h_e/d and H_1/d is not straightforward. This is primarily because of the presence of multiple equilibrium position of a heavy particle at the same Reynolds number, first detected by Choi and Joseph (2001). It was explained by Patankar et al. (2001a) to be due to the presence of a turning point bifurcation of the equilibrium solution (Fig. 4). Turning point bifurcations have also been found in computations of levitation to equilibrium of particles in viscoelastic fluids of Oldroyd-B type (Ko et al., in preparation). This implies that the correlation function in Eq. (8) will not be a single valued monotonous form. We have not observed multiple equilibrium heights of the particle bed in our many particle simulations at the parameters we tested. Hence, many particle correlations for lift in terms of a single particle variable analogous to Eq. (1) is not preferred. In the next subsection we see that it is more convenient to obtain many particle correlations similar in form to Eq. (6).

Multiple stable equilibrium positions are not observed for neutrally buoyant particles. A neutrally buoyant particle has a stable equilibrium position between the channel axis and the wall. This is known since the well-known experiments of Segré and Silberberg (1962). They found that at low Reynolds number Poiseuille flows, the equilibrium position of a sphere from the pipe axis was found to be 0.6 times the pipe radius.

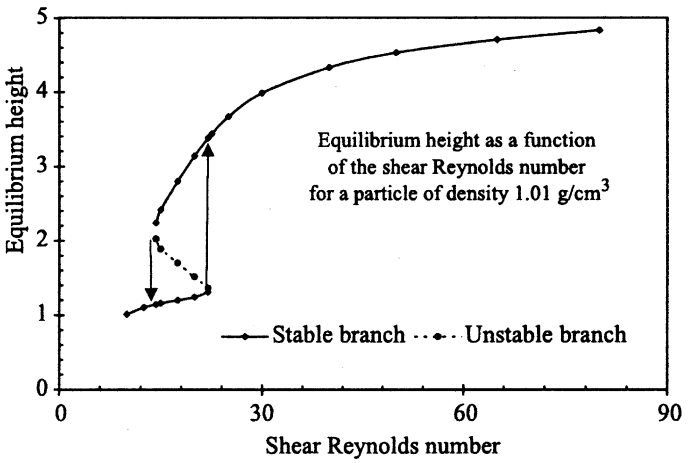

Fig. 4. Turning point "bifurcations" shown in the equilibrium height (cm) vs. Reynolds number curve. There are two stable branches separated by an unstable branch. The channel height is 12 cm (Patankar et al., 2001a).

A general expression for single particle lift force analogous to the drag formula, valid at all Reynolds numbers, has not been obtained yet. Joseph et al. (2002) have suggested that the slip angular velocity discrepancy defined as the difference between the slip angular velocity of a migrating particle and the slip angular velocity at its equilibrium position may be an important variable to model lift. It is positive below the position of equilibrium and negative above it. This discrepancy is the quantity that changes sign above and below the equilibrium position for neutrally buoyant particles, and also above and below the lower equilibrium position for heavy particles. On the other hand the translational slip velocity discrepancy does not change sign. The translational slip velocity is the fluid velocity at the particle center when there is no particle minus the particle velocity. The angular slip velocity is similarly defined.

3.2. Direct numerical simulation of levitation to equilibrium of 300 circular particles

The transport of a slurry of 300 heavier than liquid particles in a plane pressure driven flow of Newtonian fluids was studied using 2D DNS by Choi and Joseph (2001) and Patankar et al. (2001b). Particles are initially placed at the bottom of a periodic channel of height H_1 in a close packed ordered configuration. The flow is driven by an external pressure gradient. At steady condition, the particle bed reaches a constant height (Fig. 5). The height of the clear fluid region above the particle bed is H_2 and the average fluid fraction in the particle bed is ε. Similar to Eq. (8) we expect that

$$R_G = f_3\left(R, \varepsilon, \varepsilon_{max}, \frac{H_1}{d}\right), \tag{10}$$

where

$$\varepsilon = 1 - \frac{N\pi d^2}{4[H_1 - H_2]l}, \quad \varepsilon_{max} = 1 - \frac{N\pi d^2}{4H_1 l},$$

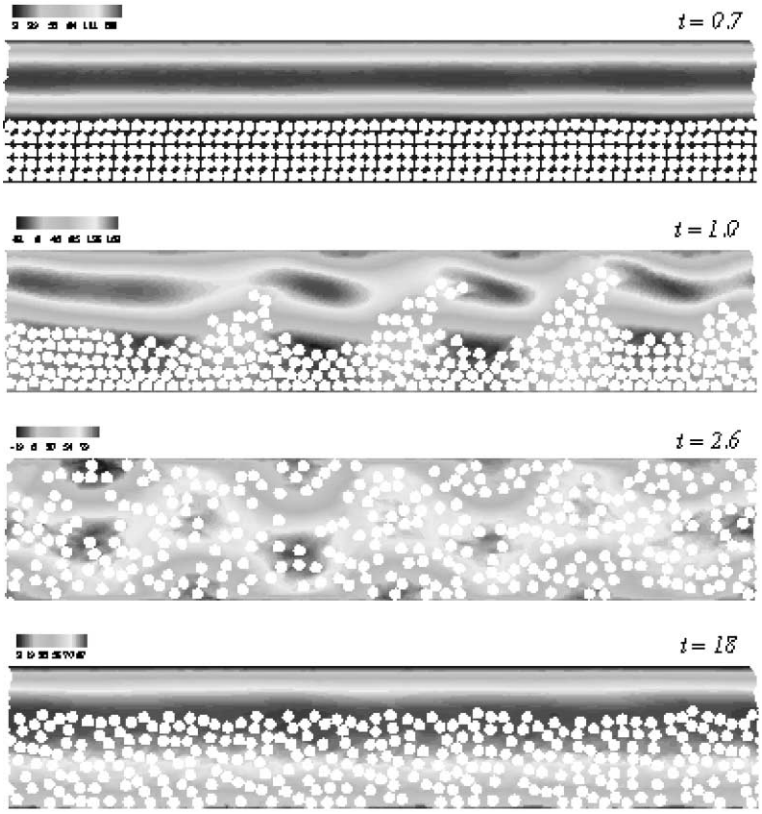

Fig. 5. Lift-off of 300 heavy particles in a plane pressure driven flow of a Newtonian fluid, $Re = 1800$. Contour plot of the horizontal velocity component is shown (Patankar et al., 2001b).

where N is the number of particles, l is the channel length and $\varepsilon_{\max}$ is the fluid fraction in the particle bed if the particles occupy the entire height of the channel, i.e. if $H_2 = 0$.

During the simulations $\varepsilon_{\max}$ and H_1/d were constant (Patankar et al., 2001b, Choi and Joseph, 2001). Therefore, R_G should be a function of R and ε only. Patankar et al. (2001b) obtained the following correlation:

$$R_G = 3.27 \times 10^{-4} \varepsilon^{-9.05} R^{1.249}, \quad \text{or}$$
$$R_G = 3.27 \times 10^{-4} \left[\frac{\varepsilon_{\max} - H_2/H_1}{1 - H_2/H_1} \right]^{-9.05} R^{1.249}. \tag{11}$$

The correlation above is of the same form as that expected from Eq. (6). This shows that fluidization of slurries by lift also falls into enabling correlations of the RZ type and the above correlation by Patankar et al. (2001b) could be called a RZ type of correlation for fluidization by lift. Lift results for fluidized slurries are power laws in appropriate dimensionless parameters. These power laws are in the form of engineering type correlations; to use them in applications we need rules for converting 2D to 3D results. The goal of our future work is to generate power laws for engineering applications by processing results of simulations in 3D just as we have done in 2D.

The DNS results are in agreement with the expected power law form in Eq. (6) from the analogy between fluidization by drag and shear. In the next sections we analyze the experimental data for proppant transport to verify the prediction of power laws from DNS.

4. Experimental setup

Kern et al. (1959) reported the earliest experimental investigation of proppant transport in narrow slots. STIM-LAB did more experiments to better understand the processes involved in proppant transport by water and other thin fluids. We have analyzed the data obtained from their experiments. The apparatus used by STIM-LAB was constructed so that the transport of proppant in a horizontally oriented slot could be observed. A schematic of the apparatus is shown in Fig. 6.

Proppant can be added at a constant rate and water flow rate is also constant. Proppant and water enter the 8 mm wide slot through an open end that is 30.5 cm tall. The proppant and water then move through the 2.44 m length of the slot where they exit via three 8 mm perforations spaced 7.62 cm apart on the 30.5 cm tall end of the slot. The proppant and water flow rates were varied, proppants of varying size and density were added and water at different temperatures was used. Observations were recorded and portions of the experiments were video taped.

The evolution of the proppant bed in the experiments is well described in Fig. 7. The portion shown in Fig. 7 is marked in Fig. 6. In the steady state there is an initial development length (see Fig. 6) followed by a flat bed region shown in Fig. 7 and marked in Fig. 6. There are three distinct zones in the flat bed region. The bottom part of the bed is immobile; it is a stationary porous medium that supports liquid throughput that might be modeled by Darcy's law. Above the

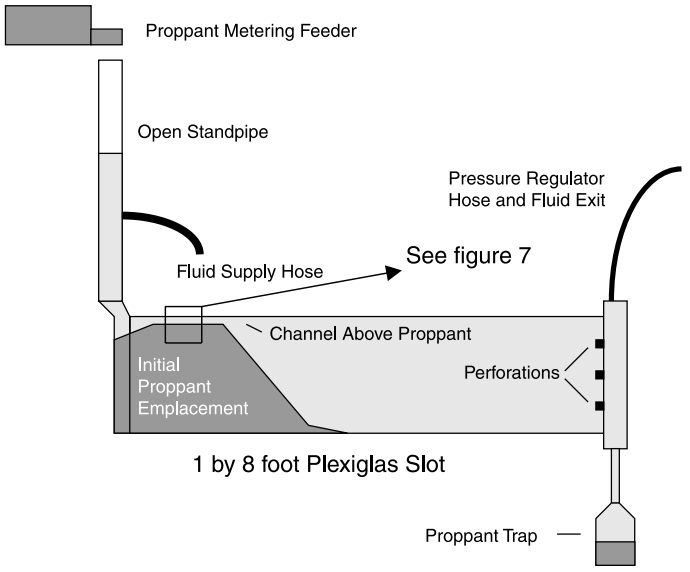

Fig. 6. The experimental setup for proppant transport. Proppant and fluid are added at the left where they enter over the full height of the slot. Materials exit at the right through perforations.

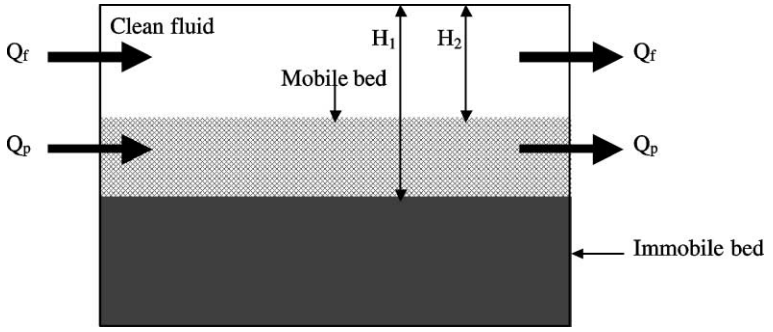

Fig. 7. Proppant transport in thin fluids at steady state conditions. In Case 1 only fluid is pumped, $Q_P = 0$, $H_1 = H_2$; the particles are immobile. In Case 2 proppants are also injected, $Q_P \neq 0$, $H_1 \neq H_2$; there is a mobile bed of height $H_1 - H_2$. The channel width $W = 8$ mm.

immobile bed is a mobile bed in which particles move by sliding and rolling or advection after suspension or a combination of these modes. Above the mobile bed is the clear fluid zone. At steady state the volumetric fluid flow rate Q_f and the volumetric proppant flow rate Q_p in and out of this region are constant. At steady state, these are equal to the rate at which the fluid and proppant are injected in the slot.

STIM-LAB carried out two types of experiments looking at the transport of proppants in thin fluids. In Case 1 only fluid is pumped, $Q_P = 0$, $H_1 = H_2$; the particles are immobile. In Case 2 proppants are also injected, $Q_P \neq 0$, $H_1 \neq H_2$; there is a mobile bed of height $H_1 - H_2$. The channel width $W = 8$ mm. A simplified description of the experiment is that a bed of proppant is eroded by the flow of water. When proppant is not injected as in Case 1, the faster the flow of water the deeper is the channel above the proppants. We are seeking to predict the height above the channel for the given fluid flow rate. In Case 2, we seek to predict both the clear fluid height as well as the mobile bed height as functions of Q_f and Q_p. In the experiments the fluid and the proppant flow rates are controlled and the heights H_1, H_2 are measured.

In the DNS of 300 particles reported by Choi and Joseph (2001) and Patankar et al. (2001b) (Fig. 5), we have a set up similar to that in Fig. 7. The value of H_1 in Fig. 7 is equivalent to the height of the channel in the simulations. In the simulations, data is obtained for a fixed value of H_1/d. This is not the case with the experimental data.

5. Experimental correlations for sediment/proppant transport

We develop combined correlations for the two cases studied experimentally by STIM-LAB.

5.1. Case 1: $H_1 = H_2 = H$

This case finds the critical condition of the initial motion of the proppant. Only fluid is injected in the channel. The particle bed is immobile. There is an equilibrium value of H corresponding to a given fluid flow rate. When the fluid flow rate is increased beyond the critical value for a given

initial height H, the proppants are eroded from the bed and washed out until a new equilibrium height H of the clear fluid region above an immobile bed is achieved for the new flow rate.

Table 1 gives the data from these experiments. The parameters of this problem are listed below:

Fluid Reynolds number based on channel width

$$R_q = \frac{\rho_f \tilde{V} W}{\eta} = \frac{\rho_f Q_f}{W\eta}, \quad \text{where } \tilde{V} = \frac{Q_f}{W^2}.$$

Gravity Reynolds number

$$R_G = \frac{\rho_f[\rho_p - \rho_f]gd^3}{\eta^2}.$$

Table 1
Data from experiments on the initiation of sediment motion (Case 1)

Proppants	d (cm)	H (cm)	η (g/cm s)	ρ_f (g/cm^3)	Q_f (cm^3/s)	ρ_p (g/cm^3)	R_G	$\tilde{V}$ (cm/s)	R_q	H/W
60/40	0.034212	1.7	0.01115	0.999	36.778	2.65	521.1645	58.37416	4184.12	2.141732
Brady	0.034212	2.3	0.01115	0.999	58.289	2.65	521.1645	92.51649	6631.36	2.897638
	0.034212	5.6	0.01115	0.999	133.295	2.65	521.1645	211.5662	15164.55	7.055118
	0.034212	7.8	0.01115	0.999	232.588	2.65	521.1645	369.1644	26460.80	9.826772
20/40	0.056043	2.3	0.01115	0.999	46.556	2.65	2290.822	73.89383	5296.48	2.897638
Ottawa	0.056043	5.2	0.01115	0.999	133.106	2.65	2290.822	211.2663	15142.90	6.551181
	0.056043	8.2	0.01115	0.999	227.542	2.65	2290.822	361.1554	25886.49	10.33071
20/40	0.06	1.4	0.01115	0.999	7.885	1.05	86.83778	12.5151	897.05	1.76378
Light beads	0.06	2	0.01115	0.999	10.409	1.05	86.83778	16.5212	1184.19	2.519685
	0.06	3.9	0.01115	0.999	31.92	1.05	86.83778	50.66353	3631.42	4.913386
	0.06	8.5	0.01115	0.999	128.438	1.05	86.83778	203.8572	14611.89	10.70866
	0.06	12	0.01115	0.999	226.217	1.05	86.83778	359.0523	25735.84	15.11811
16/20	0.094946	1.5	0.01	0.998	31.542	2.73	14513.72	50.06356	3997.08	1.889764
Carbolite	0.094946	2.2	0.01	0.998	50.467	2.73	14513.72	80.10138	6395.30	2.771654
	0.094946	9.9	0.01	0.998	258.642	2.73	14513.72	410.5174	32775.74	12.47244
16/20	0.094946	1.7	0.00378	0.972	36.778	2.73	100415.8	58.37416	12008.41	2.141732
Carbolite	0.094946	2.3	0.00378	0.972	58.289	2.73	100415.8	92.51649	19031.98	2.897638
	0.094946	5.6	0.00378	0.972	133.295	2.73	100415.8	211.5662	43522.25	7.055118
	0.094946	7.8	0.00378	0.972	232.588	2.73	100415.8	369.1644	75942.48	9.826772
16/30	0.088437	0.4	0.01115	0.999	10.535	3.45	13363.76	16.72119	1198.53	0.503937
Banrite	0.088437	0.6	0.01115	0.999	13.878	3.45	13363.76	22.02721	1578.85	0.755906
	0.088437	1.3	0.01115	0.999	29.145	3.45	13363.76	46.25904	3315.71	1.637795
	0.088437	3.5	0.01115	0.999	100.681	3.45	13363.76	159.8012	11454.08	4.409449
	0.088437	8.3	0.01115	0.999	261.796	3.45	13363.76	415.5234	29783.50	10.45669
12/20	0.109021	1.3	0.01015	0.998	28.955	2.65	20342.9	45.95747	3615.03	1.637795
Badger	0.109021	2.5	0.01015	0.998	62.137	2.65	20342.9	98.62404	7757.81	3.149606
	0.109021	5.8	0.01015	0.998	155.185	2.65	20342.9	246.3101	19374.85	7.307087
	0.109021	9	0.01015	0.998	290.814	2.65	20342.9	461.5809	36308.13	11.33858

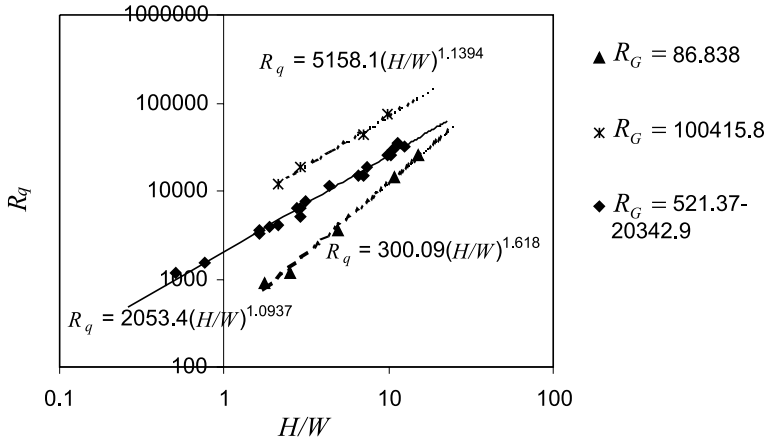

Fig. 8. Plot of R_q vs. H/W at different values of R_G on a logarithmic scale.

Particle diameter/channel width: d/W.
Height H/channel width: H/W.
Fig. 8 shows a plot of R_q vs. H/W at different values of R_G.
From Fig. 8 we get the following form for the correlation of the initiation of sediment motion:

$$R_q = a[H/W]^n, \tag{12}$$

where a and n are function of R_G. We see that a and n may be regarded as constants for $521.37 \leqslant R_G \leqslant 20342.9$. The values of a and n listed in Fig. 8 are plotted in Fig. 9a and b, respectively.
We define an effective Reynolds number as

$$R_{eff} = R_q[W/H]^n, \tag{13}$$

where the values of n are given in Fig. 8 and plotted in Fig. 9b. This leads to the following expression for the critical effective Reynolds number R_{eff}^{cr} for the initiation of bed motion

$$R_{eff}^{cr} = a(R_G). \tag{14}$$

The value of a is given in Fig. 8 and plotted in Fig. 9a. R_{eff} may be regarded as a Reynolds number that accounts for the effect of the side walls of the channel.

Shields (1936) curve also gives the critical condition for the initiation of sediment motion. The Shields parameter S is defined as $S = \tau/[\rho_p - \rho_f]gd$, where τ is a measure of the shear stress on the particle bed. If we take $\tau = \eta\tilde{V}/W$, then $S = \eta\tilde{V}/[\rho_p - \rho_f]gd^2 = R_q[d/W]/R_G$. From the Shields (1936) curve one obtains (see also, Vanoni, 1975) $S = f_s(\sqrt{R_q}[d/W])$. Eq. (14), applicable for proppant transport in narrow channels has W/H as another parameter.

5.2. Case 2: $H_1 \neq H_2$

There are two sets of data for Case 2:

1. 20/40 Ottawa sand: The parameters are given in Table 2.
2. 16/30 Carbolite sand: The parameters are given in Table 3.

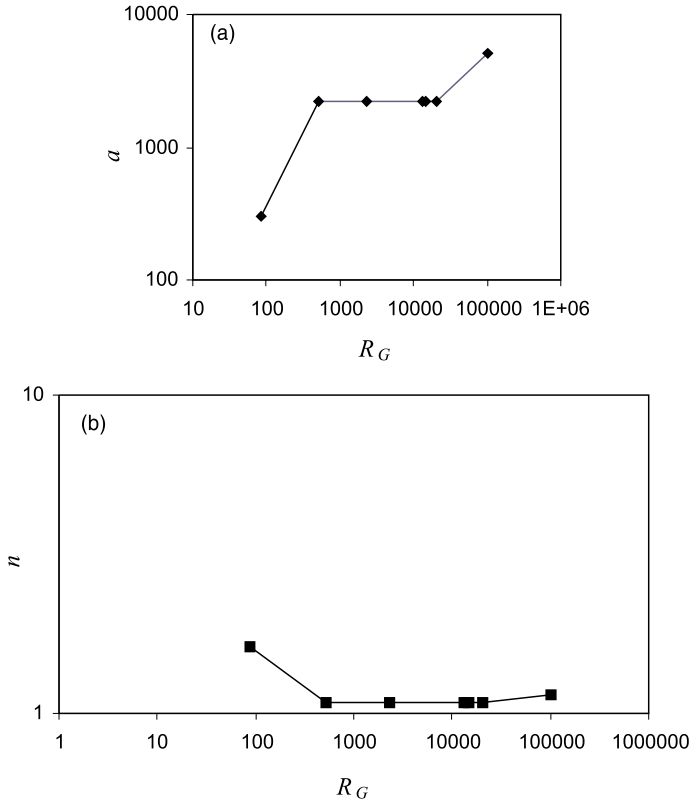

Fig. 9. (a) Plot of a vs. R_G on a logarithmic scale. (b) Plot of n vs. R_G on a logarithmic scale.

Table 2
Parameters for experiments with 20/40 Ottawa sand in Case 2

ρ_p	2.65 g/cm^3
d	0.06 cm
ρ_f	1 g/cm^3
η	0.01 g/cm s
W	0.8 cm
R_G	3496

Table 3
Parameters for experiments with 16/30 Carbolite sand in Case 2

ρ_p	2.71 g/cm^3
d	0.09 cm
ρ_f	1 g/cm^3
η	0.01 g/cm s
W	0.8 cm
R_G	12 229

In this case the fluid and the proppant are both injected at a specified volumetric flow rate. Since the proppants are injected, there is a moving particle bed in the channel. At equilibrium there is a clear fluid region of height H_2 above a moving bed of height $H_1 - H_2$. The experimental data are given in Tables 4 and 5.

First we wish to obtain a correlation for the fluid Reynolds number R_q in terms of R_G and ε. It is more convenient to obtain experimental correlations in terms of H_1 and H_2 instead of ε. Power laws in terms of H_1/H_2 were also obtained from numerical simulations (Eq. (11)).

A correlation obtained for Case 2 should reduce to the correlation for Case 1 when $H_1 = H_2$. From Case 1 we see that when $R_G = 3496$ (Ottawa) and 12229 (Carbolite) the critical effective Reynolds number $R_{\text{eff}}^{\text{cr}} = 2053.4$ and $n = 1.0937$. We define an effective Reynolds number at the fluid–proppant-bed interface as $R_{\text{eff}} = R_q(W/H_2)^{1.0937}$ for the Carbolite and Ottawa data. This is consistent with the definition of R_{eff} in Eq. (13) since H_2 is the height of the clear fluid region. Fig. 10 shows a plot of R_{eff} vs. $\ln(H_1/H_2)$ for the combined Carbolite and Ottawa data.

Two regimes are observed for the given values of R_G:

$$\text{Regime 1}: \quad R_{\text{eff}} - R_{\text{eff}}^{\text{cr}} = 26838 \ln(H_1/H_2). \tag{15}$$

$$\text{Regime 2}: \quad R_{\text{eff}} = 8177(H_1/H_2)^{1.1648}. \tag{16}$$

Note that the y-intercept is taken to be equal to $R_{\text{eff}}^{\text{cr}}$. Regime 1 shows logarithmic behavior whereas Regime 2 shows power law behavior. When $H_1/H_2 = 1$, we recover the correlation in Eq. (14). Thus Eqs. (15) and (16) represent a combined correlation for the data from Cases 1 and 2. Regimes 1 and 2 have an overlap region; we may estimate the transition to begin at $R_{\text{eff}} = 20\,000$.

The following general form of the correlation may be proposed:

$$\left(\frac{\rho_f Q_f}{H_2 \eta}\right)(W/H_2)^{n-1} - a(R_G) = 26838 \ln(H_1/H_2); \text{ Regime 1}, \tag{17}$$

Table 4
Experimental data for Case 2 with Ottawa sand

H_1 (cm)	H_2 (cm)	Q_p (cm^3/s)	Q_f (cm^3/s)	$Q = Q_p + Q_f$ (cm^3/s)	Q_p/Q	Q_f/Q
2.3	0.8	40	244.1	284.1	0.140795	0.859205
2.6	0.7	45.7	242.9	288.6	0.158351	0.841649
2.3	1	28.6	250.4	279	0.102509	0.897491
2.4	1.5	11.4	249.8	261.2	0.043645	0.956355
3	2.1	11.4	313.5	324.9	0.035088	0.964912
2.9	1.5	34.3	304.7	339	0.10118	0.89882
3.1	2.3	11.4	314.8	326.2	0.034948	0.965052
3	1.4	45.7	303.4	349.1	0.130908	0.869092
3	1.5	40	305.3	345.3	0.115841	0.884159
2.9	1.6	28.6	306	334.6	0.085475	0.914525
2.8	1.7	22.8	306	328.8	0.069343	0.930657
3.1	2	17.1	315.4	332.5	0.051429	0.948571
3.5	2.9	5.7	314.2	319.9	0.017818	0.982182
4.1	3.6	2.9	313.5	316.4	0.009166	0.990834
5.1	5	1.4	312.9	314.3	0.004454	0.995546
5.8	5.7	0.4	311.6	312	0.001282	0.998718

Table 5
Experimental data for Case 2 with Carbolite sand

H_1 (cm)	H_2 (cm)	Q_p (cm^3/s)	Q_f (cm^3/s)	$Q = Q_p + Q_f$ (cm^3/s)	Q_p/Q	Q_f/Q
2	1.2	11.2	180.4	191.6	0.058455	0.941545
2.1	1.2	16.8	180.4	197.2	0.085193	0.914807
1.7	0.5	22.3	180.4	202.7	0.110015	0.889985
1.9	0.6	27.9	180.4	208.3	0.133941	0.866059
1.9	0.4	33.5	180.4	213.9	0.156615	0.843385
1.7	0.2	44.7	180.4	225.1	0.198578	0.801422
2.4	1.5	5.6	192.4	198	0.028283	0.971717
2.8	2.1	2.8	193.7	196.5	0.014249	0.985751
3	2.8	1.4	193.7	195.1	0.007176	0.992824
3.3	2.8	0.7	195.6	196.3	0.003566	0.996434
4.3	3.9	0.3	195.6	195.9	0.001531	0.998469
2.9	1.6	22.3	306.6	328.9	0.067802	0.932198
2.9	2	11.2	307.2	318.4	0.035176	0.964824
3.3	2.6	5.6	306	311.6	0.017972	0.982028
4	3.2	2.8	309.7	312.5	0.00896	0.99104
4	3.2	1.4	311	312.4	0.004481	0.995519
4.2	3.5	0.7	311	311.7	0.002246	0.997754
5.3	5	0.3	316	316.3	0.000948	0.999052
3.1	1	44.7	315.4	360.1	0.124132	0.875868
3	1.2	39.1	314.2	353.3	0.110671	0.889329
3	1.3	33.5	308.5	342	0.097953	0.902047
3	1.3	27.9	310.5	338.4	0.082447	0.917553
2.9	1.6	22.3	309.1	331.4	0.06729	0.93271
3	1.8	16.8	312.1	328.9	0.051079	0.948921
3.2	2.1	11.2	318.6	329.8	0.03396	0.96604
3.4	2.6	5.6	321.1	326.7	0.017141	0.982859
3.5	2.9	4.2	316	320.2	0.013117	0.986883

and

$$\left(\frac{\rho_f Q_f}{H_2 \eta}\right)(W/H_2)^{n-1} = 8177(H_1/H_2)^{1.1648};\ \text{Regime 2.} \tag{18}$$

Eqs. (15) and (16) can also be represented by a single equation using a technique described in Appendix A by R.D. Barree. The single equation is given by

$$R_{\text{eff}} = \frac{8177(H_1/H_2)^{1.1648}}{\left(1 + \left(\frac{H_1/H_2}{0.9}\right)^{-9}\right)^{5}}. \tag{19}$$

Eq. (19) implies that correlations in the entire range can be represented by power laws connected by transition regions. The logarithmic regime could be regarded as the 'transition type' region.

The above correlation suggests the following model for proppant transport. Consider some experiment with a channel of given height H_2 and width W. Begin the fluid flow in the channel. After a critical value Q_f, obtained from Eq. (14), the fluid begins to move or erode the proppant in

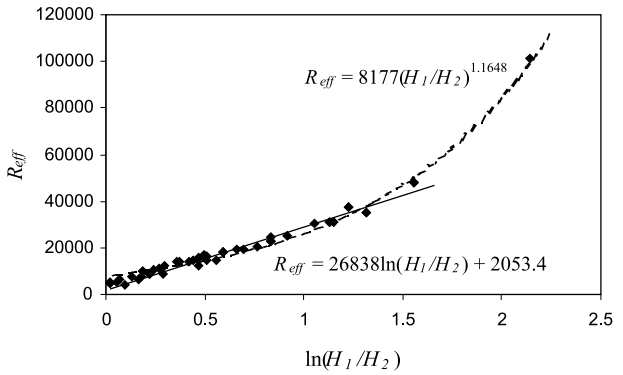

Fig. 10. Plot of R_{eff} vs. $\ln(H_1/H_2)$ for the combined Carbolite and Ottawa data.

the bed. This results in a proppant flow rate corresponding to the given values of Q_{f} and H_2. The height H_2 remains almost the same but the depth $H_1 - H_2$ increases as the fluid flow rate is increased. The depth H_1 to which the bed moves can be found from Eq. (15). This is Regime 1 or the bed erosion regime. This regime may also be regarded as the bed-load transport regime. The correlation suggests a logarithmic behavior in the bed erosion regime.

Further increase in the fluid flow rate induces suspension of the particles, hence the bed begins to 'inflate' or 'expand'. This situation is identical to our numerical simulations. Bed expansion now causes the value of H_2 to decrease. This is Regime 2 or the bed expansion regime. As expected from our numerical simulation results, the experimental data also shows power law relation between the fluid Reynolds number and H_1/H_2. The forms of numerical and experimental correlations are not identical obviously due to additional complexities such as three dimensionality and narrow slot in the case of experiments. Nevertheless, we observe that a power law behavior lies at the foundation of these flows.

In order to obtain a fully predictive model another correlation for the proppant flow rate is required. We found that the data correlates best with a non-dimensional variable R_{p} for proppant flow rate given by $R_{\text{p}} = \rho_{\text{f}} Q_{\text{p}}/H_1\eta$. The data is plotted in Fig. 11.

Once again we observe two regimes consistent with those in Fig. 10. The correlations are

$$\text{Bed erosion regime}: \quad R_{\text{eff}} - R_{\text{eff}}^{\text{cr}} = 1057.7 R_{\text{p}}^{0.397} \tag{20}$$

$$\text{Bed expansion regime}: \quad R_{\text{eff}} - R_{\text{eff}}^{\text{cr}} = 0.0356 R_{\text{p}}^{1.8522}. \tag{21}$$

The transition point is around $R_{\text{eff}} = 20000$. Using a technique presented in Appendix A by R.D. Barree, Eqs. (20) and (21) can be given by a single equation representing power laws connected by transition regions

$$R_{\text{eff}} - R_{\text{eff}}^{\text{cr}} = \frac{1057.7 R_{\text{p}}^{0.397}}{\left(1 + \left(\frac{R_{\text{p}}}{1185.07}\right)^5\right)^{-0.291}}. \tag{22}$$

Eqs. (15)–(22) represent correlations for proppant transport in a narrow channel. Power laws are observed in agreement with the expectation from numerical results and the analogy between

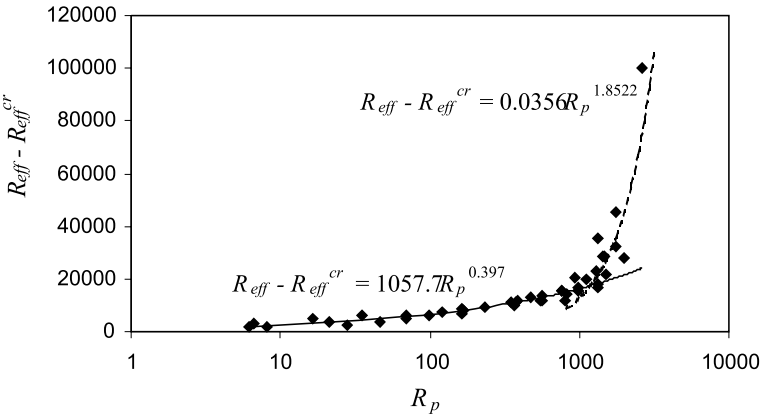

Fig. 11. Plot of $R_{\mathrm{eff}} - R_{\mathrm{eff}}^{\mathrm{cr}}$ vs. R_{p}.

fluidization by drag and lift. The correlations in Eqs. (15)–(22) can be used as a predictive tool, e.g. to obtain the values of H_1 and H_2 for given values of fluid and proppant flow rates. A correlation in terms of ε, giving an expression identical to the form in Eq. (6), may be desirable to develop models for sediment transport for use in simulators. We are currently investigating this aspect further.

The prediction of the transition point between the bed erosion and bed expansion regimes may require further experimental and numerical investigation. Typically, our data fit curves have a coefficient of determination (the R-squared value) of 0.93–0.99 (1 being the ideal case); exception being Eq. (21) where the R-squared value is 0.7. Clearly, further experimental investigation is required for that regime.

The power law fits we have obtained are valid for moderate to high Reynolds number cases. Different exponents are expected in the low Reynolds number regime (particle Reynolds numbers less than 1).

The correlations in Eqs. (19) and (22) are fully predictive, i.e. there are two equations for two unknowns H_1 and H_2. These two equations are power laws. It is emphasized here, that more data is required to develop generalized expression. Some exponents and prefactors that appear as constants in the correlations (Eqs. (19) and (22)) need not be so and may be functions of parameters like R_{G} in generalized expressions. In this work we have shown that the available data leads to power law correlations for lift. Similar behavior should be expected from additional data.

6. Conclusions

We believe that research leading to optimal techniques of processing data for correlations from real and numerical experiments is founded on the far from obvious property of self-similarity (power laws) in the flow of dispersions. The basis for this belief are the excellent correlations of experiments on fluidization and sedimentation done by Richardson and Zaki and the correlations for sediment transport in horizontal channels obtained from our numerical simulations and the analysis of the experimental data from STIM-LAB.

Results of 2D simulations of solid–liquid flows give rise to straight lines in log–log plots of the relevant dimensionless Reynolds numbers. Power laws are also obtained from the analysis of experimental data. The extent and apparent universality of this property is remarkable and shows that the flow of these dispersions are governed by a hidden property of self-similarity leading to power laws. These power laws make a powerful connection between sophisticated high performance computation, experiments and the world of engineering correlations.

The correlations obtained can be used as predictive tools or as a basis for models for sediment transport in simulators used for design purposes.

Acknowledgements

We acknowledge support by the National Science Foundation KDI/New Computational Challenge grant (NSF/CTS 98-73236), by the DOE, Department of Basic Energy Sciences, by a grant from the Schlumberger foundation, from STIM-LAB Inc. and by the Minnesota Supercomputer Institute. NAP acknowledges the support from Northwestern University through startup funds.

Appendix A. Fitting power law data with transition regions by a continuous function: General framework and application to the RZ correlation

Many data sets representing naturally occurring phenomena can be described using a sigmoidal distribution function. One such function that is particularly useful in fitting physical data is the logistic dose–response curve given by

$$y = a + \frac{(b-a)}{\left(1+\left(\frac{x}{t}\right)^{c}\right)^{d}}. \tag{A.1}$$

In this equation each of the constant terms or coefficients (a, b, c, d and t) have readily apparent physical significance, which allows data modeling to be accomplished almost by inspection.

Fig. 12 shows the dose–response function for $a = 1$, $b = 1000$, $c = 2$, $d = 1$, and $t = 10$. As can be seen, the coefficients a and b represent the values of the lower and upper plateaus of the function, respectively, or its range. The coefficient t defines the value of the independent variable (x) where the function deviates from the constant first plateau value. The sharpness of curvature during the deviation from the first plateau is determined by the coefficient c. The slope of the power law straight line in transition from the first plateau to the second plateau is determined by the product of coefficients c and d. The slope in this example is negative because both exponents are positive in the denominator of the rational fraction.

The effects of changing the signs of the exponents can be examined (Fig. 13). If the sign of coefficient c is changed, the plot is essentially rotated about a line parallel to the y-axis through the transition value t (compare curves A and B in Fig. 13). If the sign of the coefficient d is changed, the plot is rotated about a line parallel to the x-axis through the upper bound b (compare curves A and C in Fig. 13). These relationships allow construction of a transition function in any general

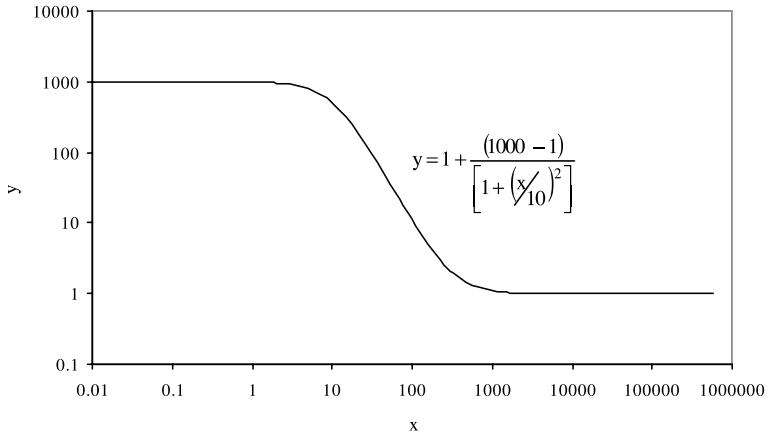

Fig. 12. A typical logistic dose–response curve.

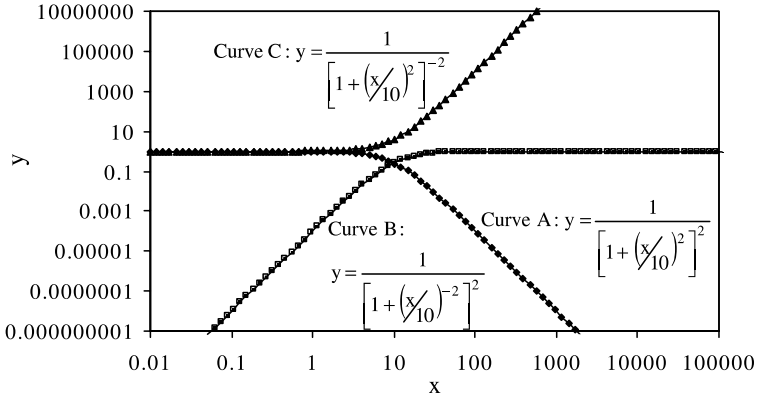

Fig. 13. Effects of changing signs of coefficients c and d in the logistic dose–response curve.

form. Another useful property of this function is that the bound corresponding to the coefficient a can be eliminated by setting its value to zero. With $a = 0$ the function yields a horizontal line at the upper bound value b and a power law line of slope cd which extends to infinity (Curve A, Fig. 13). Various functions can then be modeled by products of functions with specified power law slopes and transition points (Fig. 14). For curve A in Fig. 14 $c_1 = 2$, $d_1 = 1$ and for curve B $c_2 = 1.6$, $d_2 = -1$. The final power law slope in the product is then $c_1 d_1 + c_2 d_2$.

Combinations of these functions can be used in various forms to model many commonly observed phenomena. The logistic dose–response curve can also be multiplied by a linear power law function to impose an overall slope to the function. Quite complex systems can be modeled by combining rational fractions or products of multiple functions.

This method has been used to model the RZ correlation that relates bed fluidization velocity to the solids volume-fraction of particles in suspension. The RZ correlation is given by Eq. (1). Specifically, the various functions representing the exponent n are (Richardson and Zaki, 1954)

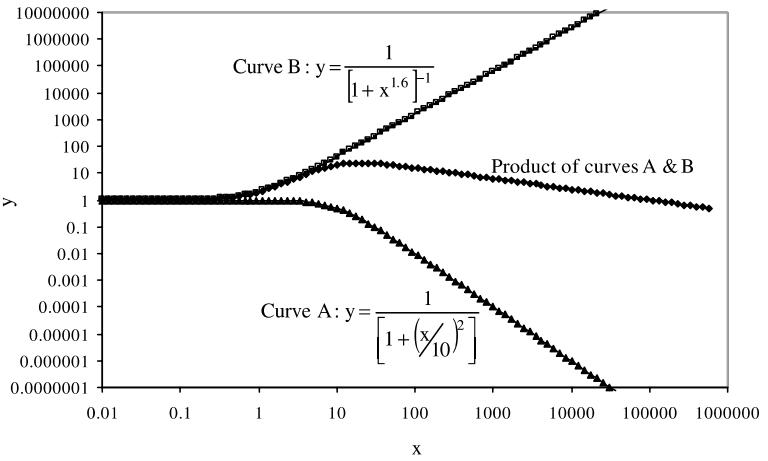

Fig. 14. Obtaining a curve from the product of two different logistic dose–response curves.

$$
\begin{aligned}
n &= \left(4.65 + 19.5\frac{d}{D}\right) \quad \text{when } R_0 < 0.2,\\
n &= \left(4.35 + 17.5\frac{d}{D}\right)R_0^{-0.03} \quad \text{when } 0.2 < R_0 < 1,\\
n &= \left(4.45 + 18\frac{d}{D}\right)R_0^{-0.1} \quad \text{when } 1 < R_0 < 200,\\
n &= 4.45R_0^{-0.1} \quad \text{when } 200 < R_0 < 500,\\
n &= 2.39 \quad \text{when } 500 < R_0,
\end{aligned}
\tag{A.2}
$$

In these relations d is particle diameter, and D is the diameter of the fluidization column. Note that in Eq. (A.2) the value of n at the transition points is not unique. Nevertheless, these functions

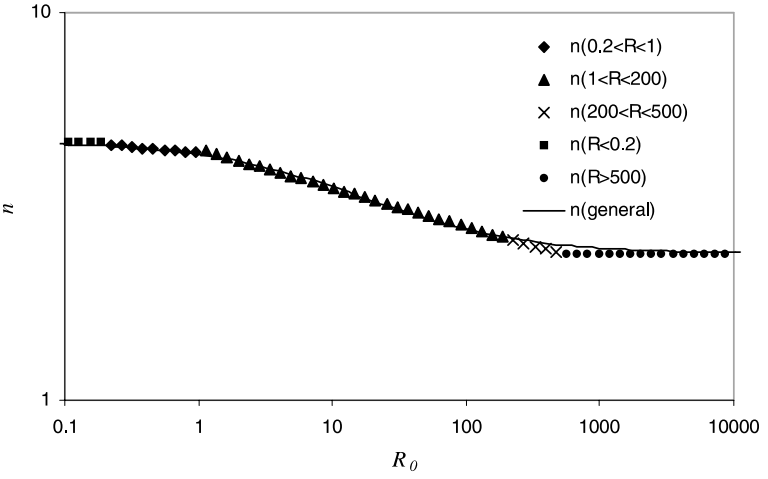

Fig. 15. A continuous logistic dose–response curve for the RZ exponent n for $d/D = 0$.

can be replaced with a single continuous form of the logistic dose–response curve where R_0 is the independent variable and n is the dependent result (Fig. 15).

Fig. 15 shows a continuous curve for the RZ exponent n. The continuous form of the function is formed assuming that n should not decrease below a value of 2.39 for any value of Re. The continuous form is generated by the equation

$$n = 2.39 + \frac{(2.26 + 19.5d/D)}{\left[1 + \left(\frac{R_0}{T}\right)^{0.7}\right]^{1.1}}. \tag{A.3}$$

This function sets a minimum value of $n = 2.39$ and a maximum that is a function of the ratio of particle size to vessel diameter (first of Eq. (A.2)). The transition value T is also a weak function of the diameter ratio d/D, and is given by

$$T = 1 + \frac{12.0}{\left(1 + \left(\frac{d/D}{0.1}\right)\right)}. \tag{A.4}$$

The final calculation of n is then given by a combination of Eqs. (A.3) and (A.4). Rowe (1987) obtained an empirical equation for the RZ exponent by using the logistic curve for $d/D = 0$. We verified that there is good quantitative agreement between Eq. (A.3) (for $d/D = 0$) and Rowe's equation.

The above technique has been applied to obtain Eqs. (19) and (22) for proppant transport in horizontal channels.

References

Asmolov, E.S., 1990. Dynamics of a spherical particle in a laminar boundary layer. Fluid Dyn. 25, 886–890.

Asmolov, E.S., 1999. The inertial lift on a spherical particle in a plane Poiseuille flow at large channel Reynolds number. J. Fluid Mech. 381, 63–87.

Auton, T.R., 1987. The lift force on a spherical body in a rotational flow. J. Fluid Mech. 183, 199–218.

Bagnold, R.A., 1966. An approach to the sediment transport problem for general physics. Geological Survey Prof. Paper 422-I, Washington, DC.

Bagnold, R.A., 1974. Fluid forces on a body in shear-flow: experimental use of stationary flow. Proc. R. Soc. London A 340, 147–171.

Barenblatt, G.I., 1996. Scaling, Self Similarity and Intermediate Asymptotics. Cambridge University Press, Cambridge.

Bretherton, F.P., 1962. Slow viscous motion round a cylinder in a simple shear. J. Fluid Mech. 12, 591–613.

Celik, I., Rodi, W., 1991. Suspended sediment-transport capacity for open channel flow. J. Hydr. Engrg. ASCE 117, 191–204.

Cherukat, P., McLaughlin, J.B., Dandy, D.S., 1999. A computational study of the inertial lift on a sphere in a linear shear flow field. Int. J. Multiphase Flow 25, 15–33.

Choi, H.G., 2000. Splitting method for the combined formulation of fluid–particle problem. Comput. Meth. Appl. Mech. Engrg. 190, 1367–1378.

Choi, H.G., Joseph, D.D., 2001. Fluidization by lift of 300 circular particles in plane Poiseuille flow by direct numerical simulation. J. Fluid Mech. 438, 101–128.

Chorin, A.J., 1968. Numerical solution of the Navier–Stokes equations. Math. Comput. 22, 745–762.

Dandy, D.S., Dwyer, H.A., 1990. A sphere in shear flow at finite Reynolds number: effect of shear on particle lift, drag and heat transfer. J. Fluid Mech. 216, 381–410.

Drew, D.A., Passman, S.L., 1999. Theory of Multicomponent Fluids. Springer-Verlag, New York.

Eichhorn, R., Small, S., 1964. Experiments on the lift and drag of spheres suspended in a Poiseuille flow. J. Fluid Mech. 20, 513–527.

Foscolo, P.V., Gibilaro, L.G., 1984. A fully predictive criterion for transition between particulate and aggregate fluidization. Chem. Engrg. Sci. 39, 1667–1675.

Hogg, A.J., 1994. The inertial migration of non-neutrally buoyant spherical particles in two-dimensional flows. J. Fluid Mech. 272, 285–318.

Hu, H.H., 1996. Direct simulation of flows of solid–liquid mixtures. Int. J. Multiphase Flow 22, 335–352.

Hu, H.H., Patankar, N.A., Zhu, M.Y., 2001. Direct numerical simulations of fluid–solid systems using the Arbitrary-Lagrangian–Eulerian technique. J. Comp. Phys. 169, 427–462.

Joseph, D.D., 1990. Generalization of the Foscolo–Gibilaro analysis of dynamic waves. Chem. Engrg. Sci. 45, 411–414.

Joseph, D.D., 2002. Interrogations of direct numerical simulation of solid–liquid flow. Available from <http://www.aem.umn.edu/Solid–Liquid_Flows>.

Joseph, D.D., Ocando, D., 2002. Slip velocity and lift. J. Fluid Mech. 454, 263–286.

Kern, T.K., Perkins, T.K., Wyant, R.E., 1959. The mechanics of sand movement in fracturing. Petrol. Trans. AIME 216, 403–405.

Ko, T., Patankar, N.A., Joseph, D.D., in preparation. Multiple equilibrium positions in the lift-off of a single particle in Newtonian and viscoelastic fluids.

Krishnan, G.P., Leighton, D.T., 1995. Inertial lift on a moving sphere in contact with a plane wall in a shear flow. Phys. Fluids 7, 2538–2545.

Kurose, R., Komori, S., 1999. Drag and lift forces on a rotating sphere in a linear shear flow. J. Fluid Mech. 384, 183–206.

Leighton, D.T., Acrivos, A., 1985. The lift on a small sphere touching a plane in the presence of a simple shear flow. Z. Angew. Math. Phys. 36, 174–178.

McLaughlin, J.B., 1991. Inertial migration of a small sphere in linear shear flows. J. Fluid Mech. 224, 261–274.

Mei, R., 1992. An approximate expression for the shear lift force on a spherical particle at finite Reynolds number. Int. J. Multiphase Flow 18, 145–147.

Morris, J.F., Brady, J.F., 1998. Pressure-driven flow of a suspension: buoyancy effects. Int. J. Multiphase Flow 24, 105–130.

Pan, T.W., Joseph, D.D., Bai, R., Glowinski, R., Sarin, V., in press. Fluidization of 1204 spheres: simulation and experiment. J. Fluid Mech.

Patankar, N.A., Huang, P.Y., Ko, T., Joseph, D.D., 2001a. Lift-off of a single particle in Newtonian and viscoelastic fluids by direct numerical simulation. J. Fluid Mech. 438, 67–100.

Patankar, N.A., Ko, T., Choi, H.G., Joseph, D.D., 2001b. A correlation for the lift-off of many particles in plan Poiseuille of Newtonian fluids. J. Fluid Mech. 445, 55–76.

Richardson, J.F., Zaki, W.N., 1954. Sedimentation and fluidization: Part I. Trans. Instn. Chem. Engrg. 32, 3553.

Rowe, P.N., 1987. A convenient empirical equation for estimation of the Richardson–Zaki exponent. Chem. Engrg. Sci. 42, 2795–2796.

Rubinow, S.I., Keller, J.B., 1961. The transverse force on a spinning sphere moving in a viscous fluid. J. Fluid Mech. 11, 447–459.

Saffman, P.G., 1965. The lift on a small sphere in a slow shear flow. J. Fluid Mech. 22, 385–400; and Corrigendum 1968 J. Fluid Mech. 31, 624.

Shields, A., 1936. Anwendung der aenlichkeitsmechanik und der turbulenzforschung auf die geschiebebewegung. Mitteilungen der Preussischen Versuchsanstalt fur Wasserbau und Schiffbau, Berlin, Germany (W.P. Ott, J.C. Uchelen, Trans.). California Institute of Technology, California.

Schonberg, J.A., Hinch, E.J., 1989. Inertial migration of a sphere in Poiseuille flow. J. Fluid Mech. 203, 517–524.

Segr, G., Silberberg, A., 1962. Behavior of macroscopic rigid spheres in Poiseuille flow. 2. Experimental results and interpretation. J. Fluid Mech. 14, 136–157.

Sumer, B.M., 1986. Recent developments on the mechanics of sediment suspension. In: Bechtelered, W. (Ed.), Transport of Suspended Solids in Open Channels. Euromech 192, Neubiberg, Balkema, Rotterdam, The Netherlands, pp. 3–13.

Vanoni, V.A., 1975. Factors determining bed forms of allovial streams. J. Hydr. Eng. Div. ASCE 101, 1435–1440.
van Rijn, L.C., 1984a. Sediment transport. I. Bed load transport. J. Hydr. Engrg. ASCE 110, 1431–1456.
van Rijn, L.C., 1984b. Sediment transport. II. Suspended load transport. J. Hydr. Engrg. ASCE 110, 1613–1641.
Ye, J., Roco, M.C., 1992. Particle rotation in a Couette flow. Phys. Fluids A 4, 220–224.